

Single-particle and many-body analyses of a quasi-disordered integrable system after a quench

Kai He,^{1,2} Lea F. Santos,³ Tod M. Wright,⁴ and Marcos Rigol¹

¹*Department of Physics, The Pennsylvania State University, University Park, Pennsylvania 16802, USA*

²*Department of Physics, Georgetown University, Washington, DC 20057, USA*

³*Department of Physics, Yeshiva University, New York, NY 10016, USA*

⁴*The University of Queensland, School of Mathematics and Physics, Queensland 4072, Australia*

In general, isolated integrable quantum systems relax to an apparent equilibrium state in which the expectation values of few-body observables are described by the generalized Gibbs ensemble. However, recent work has shown that relaxation to such a generalized statistical ensemble can be precluded by localization in the presence of (quasi-)disorder. Here we undertake complementary single-particle and many-body analyses of noninteracting spinless fermions and hard-core bosons within the Aubry-André model to gain insight into this phenomenon. Our investigations span both the localized and delocalized regimes of the quasi-disordered system, as well as the critical point separating the two. Considering first the case of spinless fermions, we study the dynamics of the momentum distribution function and characterize the effects of real-space and momentum-space localization on the relevant single-particle wavefunctions and correlation functions. We show that although some observables do not relax in the delocalized and localized regimes, the observables that do relax in these regimes do so in a manner consistent with a recently proposed Gaussian equilibration scenario, whereas relaxation at the critical point has a more exotic character. We also construct various statistical ensembles from the many-body eigenstates of the fermionic and bosonic Hamiltonians and study the effect of localization on their properties.

PACS numbers: 05.30.-d, 05.70.Ln, 02.30.Ik, 05.30.Jp, 05.30.Fk

I. INTRODUCTION

In recent years, there has been a dramatic growth in interest in the physics of non-equilibrium quantum systems, driven in large part by advances in experimental atomic physics, in particular in the area of optical lattices [1, 2]. The precision time-dependent control and observation of quantum effects afforded by these experiments, together with the high degree of isolation of the system from the environment, have invigorated the theoretical study of the time evolution of isolated many-body quantum systems. The predictions of previously abstract lines of theoretical inquiry into the mechanisms by which thermal behavior emerges from purely unitary dynamics, and the role of conservation laws and integrability in such dynamics, can now for the first time be directly compared with empirical evidence acquired in experimental laboratories.

Several theoretical studies into the quantum origins of thermalization in isolated nonintegrable systems have found that away from the edges of the spectrum, few-body observables relax to the predictions of conventional statistical ensembles [3–10], which has been connected [11, 12] to the emergence of quantum chaos [13–18]. In addition, it is now well established that the highly constrained dynamics of integrable systems can in fact give rise to the relaxation of few-body observables, and that the equilibrium values of these quantities are in many cases described by the generalized Gibbs ensemble (GGE) [19–35].

The GGE is constructed by maximizing the many-body entropy [36, 37] while constraining the mean values of all integrals of motion to their expectation values in the initial state $|\psi_I\rangle$ of the system. The density matrix in the GGE takes a Gaussian form similar to that of the grand-canonical ensemble, and can be written as [19]

$$\hat{\rho}_{\text{GGE}} = \frac{1}{Z_{\text{GGE}}} e^{-\sum_s \Lambda_s \hat{I}_s}, \quad (1)$$

where $Z_{\text{GGE}} = \text{Tr}[e^{-\sum_s \Lambda_s \hat{I}_s}]$ is the GGE partition function, the \hat{I}_s are the conserved integrals of motion, and the Λ_s are the corresponding Lagrange multipliers, which are determined by the constraints $\text{Tr}[\hat{\rho}_{\text{GGE}} \hat{I}_s] = \langle \Psi_I | \hat{I}_s | \Psi_I \rangle$.

The significance of the fact that the GGE provides an accurate description of observables following relaxation can be seen by contrasting its predictions with those of the “diagonal ensemble” (DE) [5]: For any initial state $|\Psi_I\rangle$, the time evolution of an observable \hat{O} under a time-independent (integrable or non-integrable) Hamiltonian \hat{H} can be written as

$$O(\tau) = \sum_{\alpha} |C_{\alpha}|^2 O_{\alpha\alpha} + \sum_{\alpha \neq \beta} C_{\alpha}^* C_{\beta} e^{i(E_{\alpha} - E_{\beta})\tau/\hbar} O_{\alpha\beta}, \quad (2)$$

where $O(\tau) = \langle \Psi(\tau) | \hat{O} | \Psi(\tau) \rangle$, $|\Psi(\tau)\rangle = \sum_{\alpha} C_{\alpha} e^{-iE_{\alpha}\tau/\hbar} |\psi_{\alpha}\rangle$, $\hat{H}|\psi_{\alpha}\rangle = E_{\alpha}|\psi_{\alpha}\rangle$, $C_{\alpha} = \langle \psi_{\alpha} | \Psi_I \rangle$, and $O_{\alpha\beta} = \langle \psi_{\alpha} | \hat{O} | \psi_{\beta} \rangle$. The infinite-time average of the observable is therefore given by

$$\begin{aligned} \overline{O(\tau)} &= \lim_{\tau' \rightarrow \infty} \frac{1}{\tau'} \int_0^{\tau'} d\tau O(\tau) \\ &= \sum_{\alpha} |C_{\alpha}|^2 O_{\alpha\alpha} \equiv \langle \hat{O} \rangle_{\text{DE}}, \end{aligned} \quad (3)$$

which defines the expectation value of \hat{O} in the DE [5]. The DE involves as many constraints as the dimension of the many-body Hilbert space (the overlaps of the initial state with the eigenstates of \hat{H}), which grows exponentially with system size. By contrast, for models that can be mapped to noninteracting Hamiltonians, the GGE involves a number of constraints that is only polynomially large in the size of the system [19]. It may, therefore, appear surprising that the predictions of the GGE for expectation values of observables can agree with those of the DE.

From a many-body perspective, the success of the GGE can be understood as follows [28]: The eigenstates of a given integrable Hamiltonian with similar distributions of conserved quantities have similar expectation values of few-body observables (with the differences vanishing in the thermodynamic limit). Furthermore, the majority of the states that contribute to the DE have a distribution of conserved quantities similar (in a coarse-grained sense) to that of the initial state, and this is also the case for the states that contribute most strongly to the GGE. These facts imply that differences between the weights in the DE and the GGE are irrelevant and both ensembles will produce the same results for few-body observables in the thermodynamic limit [28]. This scenario can be viewed as a generalization of the eigenstate thermalization hypothesis (ETH) [3–5], and has been explored in Ref. [38] for describing observables after relaxation by means of a single representative state.

Interestingly, it has been recently shown that in an integrable system, in the presence of localization, the GGE can fail to describe observables after relaxation [33]. This effect, which parallels the breakdown of eigenstate thermalization in nonintegrable disordered lattice systems in the presence of localization [39], has been related to the localized behavior of the underlying system of noninteracting particles to which some integrable models can be mapped [30, 34, 35]. Here we gain further insights into this phenomenon by undertaking single-particle and many-body analyses of noninteracting spinless fermions and hard-core bosons. We study the dynamics of noninteracting fermions within the Aubry-André model previously studied in Ref. [33] for hard-core bosons, and show that although the fermion momentum distribution equilibrates in the localized regime, it fails to equilibrate in the delocalized one. This should be contrasted with the density profiles, which exhibit the opposite behavior, equilibrating in the delocalized regime, but not in the localized regime [33]. We find that, whenever observables do equilibrate to their GGE values, they do so in a manner consistent with the Gaussian equilibration scenario of Ref. [40]. Furthermore, we relate the failure of a given quantity to equilibrate in a certain regime to the behavior of the single-particle wavefunctions, as discussed in Refs. [30, 34, 35].

For hard-core bosons, we connect the results of Ref. [33], in which the GGE was shown to fail to describe the momentum distribution function after relaxation in the localized regime, to the single-particle results for fermions. In addition, for both hard-core bosons and spinless fermions, we study the density profiles and momentum distribution functions in the many-body eigenstates of the appropriate Hamiltonians. We focus in particular on the behavior of these quantities in the many-body eigenstates that contribute to the DE, to the microcanonical ensemble (ME), and to the microcanonical version of the GGE; i.e., the generalized microcanonical ensemble (GME) [28]. We find indications that single-particle real space localization in the localized phase and momentum space localization in the delocalized phase lead to a distinctive behavior of the many-body eigenstate expectation values of the density and the momentum distribution of the fermions, respectively. No similar effect is detected in the many-body

eigenstate expectation values of the momentum distribution of the hard-core bosons.

This paper is organized as follows. In Sec. II, we introduce the models, quench protocols, and observables studied in later sections. We also review the statistical ensembles utilized to describe observables after relaxation. The time evolution of spinless fermions following a quench is studied in Sec. III. Specifically, we examine the relaxation dynamics and time fluctuations of one-body observables, as well as properties of the single-particle eigenstates that help us understand the observed out-of-equilibrium behavior. Section IV is devoted to the study of one-particle observables in the many-body eigenstates of the bosonic and fermionic Hamiltonians. In Sec. V, we summarize our results and present our conclusions.

II. MODELS AND QUENCHES

We consider two models on a one-dimensional lattice with open boundary conditions: noninteracting spinless fermions (SFs) and hard-core bosons (HCBs). The HCB model can be mapped onto the model of SFs, by mapping it first onto a spin-1/2 chain via the Holstein-Primakoff transformation [41] and then onto SFs via the Jordan-Wigner transformation [42]. In both cases, we study the effects of an additional periodic potential, with a period incommensurate with that of the underlying lattice of the tight-binding model, which results in the well known Aubry-André model [43]. The Hamiltonians for SFs and HCBs are given by

$$\hat{H}_f = -t \sum_{j=1}^{L-1} \left(\hat{f}_j^\dagger \hat{f}_{j+1} + \text{H.c.} \right) + \lambda \sum_{j=1}^L \cos(2\pi\zeta j) \hat{n}_j^f, \quad (4)$$

and

$$\hat{H}_b = -t \sum_{j=1}^{L-1} \left(\hat{b}_j^\dagger \hat{b}_{j+1} + \text{H.c.} \right) + \lambda \sum_{j=1}^L \cos(2\pi\zeta j) \hat{n}_j^b, \quad (5)$$

respectively, where L is the length of the lattice, \hat{f}_j and \hat{f}_j^\dagger (\hat{b}_j and \hat{b}_j^\dagger) are fermionic (bosonic) annihilation and creation operators on site j , and $\hat{n}_j^f = \hat{f}_j^\dagger \hat{f}_j$ ($\hat{n}_j^b = \hat{b}_j^\dagger \hat{b}_j$) are SF (HCB) site occupation number operators. The prohibition of multiple occupancy of a single site for HCBs is enforced by the hard-core constraint $\hat{b}_j^{\dagger 2} = \hat{b}_j^2 = 0$. We denote the hopping parameter by t , and the strength of the incommensurate potential by λ . To enforce the incommensurability of the lattice potential, we use an irrational value for ζ . We select the inverse golden mean, $\zeta = (\sqrt{5} - 1)/2$, which is considered to be the most irrational number [44]. For each given system size, we take the total number of SFs (HCBs) N_f (N_b) to be $N_f = N_b \equiv N$. In what follows we set t to unity; i.e., we take t as our unit of energy, and we also set $\hbar = 1$ and the Boltzmann constant $k_B = 1$.

The fermionic Hamiltonian (4) is quadratic and therefore trivially solvable: All many-body eigenstates can be constructed as Slater determinants of the single-particle energy eigenstates in the incommensurate periodic potentials.

Although the bosonic Hamiltonian (5) is also superficially quadratic, the hard-core constraints on the bosonic creation and annihilation operators encode interactions between the bosons, precluding a *direct* diagonalization in terms of single-particle states. Nevertheless, it can be solved via the combined Holstein-Primakoff and Jordan-Wigner transformations, which implies that SF and HCB systems with Hamiltonians Eqs. (4) and (5), respectively, share the same (many-body) energy spectrum and consequently have identical thermodynamic properties. Moreover, the two models have identical site occupations $\hat{n}_j^f = \hat{n}_j^b \equiv \hat{n}_j$.

The properties of HCBs in the Aubry-André model have previously been investigated, at both zero [45, 46] and finite temperature [47]. The single-particle Aubry-André model exhibits a localization-delocalization transition at the critical potential strength $\lambda_c = 2$ [43]: All single-particle states are extended when $\lambda < \lambda_c$ and exponentially localized when $\lambda > \lambda_c$. At the critical point, the energy spectrum exhibits the fractal structure of a Hofstadter butterfly [48]. As HCBs can be mapped onto non-interacting fermions, they of course inherit this phase transition when subjected to the incommensurate Aubry-André potential. In the localized regime, correlations in the ground state of the bosonic system decay exponentially with spatial separation, and the system is said to form a Bose glass [2].

Here we study the dynamics and behavior of observables following sudden quenches of the incommensurate lattice strength λ . We select initial states $|\Psi_I\rangle$ to be the ground states of initial Hamiltonians \hat{H}_I with parameters λ_I , and the dynamics are followed under final Hamiltonians \hat{H}_F with parameters λ_F , corresponding to an instantaneous change (quench) of the lattice strength from λ_I to λ_F . We focus on one-body observables that are accessible in optical lattice experiments: the density profiles \hat{n}_j , and the momentum distribution functions

$$\hat{m}_k^f = \frac{1}{L} \sum_{j,j'=1}^L e^{ik(j-j')} \hat{f}_j^\dagger \hat{f}_{j'}, \quad (6)$$

and

$$\hat{m}_k^b = \frac{1}{L} \sum_{j,j'=1}^L e^{ik(j-j')} \hat{b}_j^\dagger \hat{b}_{j'}. \quad (7)$$

We note that although the site occupations are equal for SFs and HCBs, the off-diagonal spatial correlations, and therefore the momentum distributions, of the two systems are distinct. To calculate $\langle m_k^b \rangle$ in a pure state, we follow the approach of Refs. [49–51], while for calculations in GGE we use the methodology of Ref. [52].

Ensembles of interest

We characterize the behavior of our quasi-disordered system after relaxation following a quench by comparing it to three different statistical ensembles: DE, ME, and GME, each of which we briefly describe here.

Diagonal ensemble. The density matrix of the DE is defined by

$$\hat{\rho}_{\text{DE}} = \lim_{\tau' \rightarrow \infty} \frac{1}{\tau'} \int_0^{\tau'} d\tau |\Psi(\tau)\rangle\langle\Psi(\tau)| = \sum_{\alpha} |C_{\alpha}|^2 |\psi_{\alpha}\rangle\langle\psi_{\alpha}|, \quad (8)$$

i.e., it is diagonal in the (many-body) energy representation, and the energy eigenstates are weighted according to their overlaps with the initial state. The expectation value of an observable in this ensemble is given by Eq. (3). In various computational studies [6, 7, 28], observables after relaxation have been shown to approach the DE predictions [Eq. (3)] as the system size increases.

Microcanonical ensemble. The density matrix of the ME can be written as

$$\hat{\rho}_{\text{ME}} = \frac{1}{\mathcal{N}_{E,\delta_{\text{ME}}}} \sum_{\substack{\alpha \\ |E - E_{\alpha}| < \delta_{\text{ME}}}} |\psi_{\alpha}\rangle\langle\psi_{\alpha}|; \quad (9)$$

i.e., all eigenstates in the energy window $[E - \delta_{\text{ME}}, E_{\text{ini}} + \delta_{\text{ME}}]$ (of which there are $\mathcal{N}_{E,\delta_{\text{ME}}}$) are given equal weight. We have checked that expectation values of observables within our microcanonical calculations are robust against the exact value of δ_{ME} . To ensure this, we select δ_{ME} to be much smaller than the full spectrum width, but sufficiently large to contain many eigenstates (i.e., larger than the average level spacing at the given E). In general, $\delta_{\text{ME}} = 0.05$ for most results reported in this work.

Generalized Gibbs ensemble. The density matrix for this ensemble, which is of a similar Gaussian form to that of the grand-canonical ensemble, was already introduced in Eq. (1). We note that a recipe for constructing the appropriate conserved quantities, allowing for the extension of the GGE description to more general systems, has recently been proposed [53]. However, we make here the ‘natural’ choice for the conserved quantities, taking them to be the occupations of the single-particle eigenstates of the noninteracting SFs [19].

Generalized microcanonical ensemble. The GME is the microcanonical version of the GGE [28]. The only energy eigenstates that contribute to this ensemble are those that have distributions of the conserved quantities that are similar (in a coarse-grained sense) to that of the initial state. These eigenstates are all assigned the same weight, as in the usual ME. The density matrix of the GME therefore has the form

$$\hat{\rho}_{\text{GME}} = \frac{1}{\mathcal{N}_{\{I_s\},\delta_{\text{GME}}}} \sum_{\substack{\alpha \\ \delta_{\alpha} < \delta_{\text{GME}}}} |\psi_{\alpha}\rangle\langle\psi_{\alpha}|, \quad (10)$$

where δ_{α} measures the distance of the eigenstate $|\psi_{\alpha}\rangle$ from the target distribution of conserved quantities determined by the initial state, and $\mathcal{N}_{\{I_s\},\delta_{\text{GME}}}$ is the number of energy eigenstates within the GME window $\delta_{\alpha} < \delta_{\text{GME}}$.

In order to construct the GME, one needs to compare the distribution of conserved quantities in each of the eigenstates of \hat{H}_F with that of the initial state. Since the conserved quantities are fermion occupation numbers of single-particle energy eigenstates, their expectation values in the many-body

eigenstates $I_{s,\alpha} = \langle \psi_\alpha | \hat{I}_s | \psi_\alpha \rangle$ are either 0 or 1. By contrast, the occupations of the conserved quantities in the initial state (same as in the DE) can assume any real value between these two values; i.e., $0 \leq \langle \hat{I}_s \rangle_{\text{DE}} = \sum_\alpha |C_\alpha|^2 I_{s,\alpha} \leq 1$. To compare those distributions, in a coarse grained way, we proceed as follows [28]:

- (i) We sort the conserved quantities in such a way that $\langle \hat{I}_s \rangle_{\text{DE}}$ decreases monotonically as s increases.
- (ii) After sorting, we generate a discrete target distribution of conserved quantities from $\langle \hat{I}_s \rangle_{\text{DE}}$. For this, we interpolate $\langle \hat{I}_s \rangle_{\text{DE}}$ to find a continuous function $I(s)$ (where s can now be any real number in the interval $[0.5, L + 0.5]$), and then compute all values s_l^* satisfying $\int_{0.5}^{s_l^*} I(s) ds = 0.5$ and $\int_{s_{l-1}^*}^{s_l^*} I(s) ds = 1$ for $l > 1$. The set $\{s_l^*\}$, together with the set of corresponding weights $\{I(s_l^*)\}$, defines the target distribution.

(iii) We introduce a measure δ_α to quantify how close the distribution of each many-body eigenstate $|\psi_\alpha\rangle$ is to the target distribution. Those states with $\delta_\alpha < \delta_{\text{GME}}$ are included in the GME. The choice of δ_α is not unique. As in Ref. [28], we consider

$$\delta_\alpha = \sqrt{\frac{1}{N} \sum_{l=1}^N I(s_l^*) (s_{l,\alpha} - s_l^*)^2}, \quad (11)$$

where $s_{l,\alpha}$, with $l = 1, \dots, N$, is the number of the sorted single-particle states [see (i)] occupied in eigenstate $|\psi_\alpha\rangle$. The value chosen for δ_{GME} is the one that leads to the minimum value of the normalized absolute difference

$$D = \frac{\sum_{s=1}^L |\langle \hat{I}_s \rangle_{\text{GME}} - \langle \hat{I}_s \rangle_{\text{DE}}|}{\sum_{s=1}^L \langle \hat{I}_s \rangle_{\text{DE}}}, \quad (12)$$

between the expectation values of the conserved quantities in the GME and DE. Similarly to the microcanonical calculations, we have checked that our results are robust against small changes of δ_{GME} .

III. SINGLE-PARTICLE ANALYSIS

In Ref. [33] it was shown that, following a quench of HCBs to the localized regime of the Aubry-André model, one-body observables that depend on nonlocal correlations, such as m_k^b , do relax to time-independent values (with fluctuations vanishing in the thermodynamic limit), but these values are not consistent with the predictions of the GGE. This should be contrasted with the on-site density, whose time average agrees with the GGE results for all regimes. It was also found that the dynamics of n_j and m_k^b are qualitatively different in the delocalized and localized regimes: The momentum distribution m_k^b approaches a time-independent value with increasing system size regardless of whether the system is in the delocalized or localized regime, while n_j only exhibits such relaxation in the delocalized regime. All results for the density also apply to SFs, to which HCBs can be mapped.

Here, we begin by studying the relaxation dynamics of the momentum distribution m_k^f of SFs, which is in general completely unrelated to the momentum distribution of the corresponding system of HCBs. In fact, the GGE describes, by construction, the infinite-time averages of all one-body fermionic observables regardless of whether the single-particle states are localized or delocalized and independently of the system size. This can be straightforwardly proven by projecting $\hat{\rho}(\tau) = |\Psi(\tau)\rangle\langle\Psi(\tau)|$ onto the single-particle sector. Considering that all eigenstates of the many-body Hamiltonian are (antisymmetrized) direct products of the single particle states $|s\rangle$ in which $\hat{H}_f|s\rangle = e_s|s\rangle$, the time evolution of the one-particle density matrix can be cast in the form

$$\hat{\rho}_{\text{sp}}(\tau) = \sum_{s,s'} c_{ss'} e^{-i(e_s - e_{s'})\tau} |s\rangle\langle s'|. \quad (13)$$

In the absence of degeneracies in the single-particle spectrum (which is the case in the Aubry-André model considered here), the infinite-time average of $\hat{\rho}_{\text{sp}}(\tau)$ can be written as

$$\overline{\hat{\rho}_{\text{sp}}(\tau)} = \lim_{\tau' \rightarrow \infty} \frac{1}{\tau'} \int_0^{\tau'} d\tau \hat{\rho}_{\text{sp}}(\tau) = \sum_s c_{ss} |s\rangle\langle s|, \quad (14)$$

which is, by construction, the single-particle density matrix predicted by the GGE, as $c_{ss} = \sum_\alpha |C_\alpha|^2 I_{s,\alpha} \equiv \text{Tr}[\hat{\rho}_{\text{GGE}} \hat{I}_s]$. We emphasize, however, that this does not necessarily imply that all such observables exhibit *relaxation* to their GGE values. In particular, the results of Ref. [33] indicate that the on-site densities in the localized phase exhibit finite fluctuations about their GGE expectation values even in the thermodynamic limit.

In order to quantify how closely $m_k^f(\tau) = \langle \Psi(\tau) | \hat{m}_k^f | \Psi(\tau) \rangle$ approaches the corresponding GGE prediction, we compute the normalized difference

$$\delta m^f(\tau) = \frac{\sum_k |m_k^f(\tau) - \langle \hat{m}_k^f \rangle_{\text{GGE}}|}{\sum_k \langle \hat{m}_k^f \rangle_{\text{GGE}}}, \quad (15)$$

between the instantaneous momentum distribution at time τ and the GGE prediction for this quantity. Relaxation of m_k^f to the GGE prediction is observed if $\delta m^f(\tau)$ vanishes at long times, in the thermodynamic limit. In finite-sized numerical calculations, however, $\delta m^f(\tau)$ will always be finite, because of finite-size effects. The signature of relaxation to the GGE in our calculations is therefore that $\delta m^f(\tau)$ fluctuates about a finite average value at long times, and that this average value scales towards zero with increasing system size.

In Fig. 1, we show results for $\delta m^f(\tau)$ in quenches with $\lambda_I = 0$; i.e., a delocalized initial state (left panels), and $\lambda_I = 8$; i.e., a localized initial state (right panels). After the quench, $\lambda_F = 1$ [delocalized regime, Figs. 1(a) and 1(e)], $\lambda_F = 2$ [critical point, Figs. 1(b) and 1(f)], and $\lambda_F = 3$ and 4 [localized regime, Figs. 1(c), 1(g), and 1(d), 1(h), respectively]. The results presented correspond to three different system sizes ($L = 10, 100$, and 1000 , curves from top to bottom in each panel, and $N = L/2$), and to the same quenches and system sizes studied for HCB systems in Ref. [33].

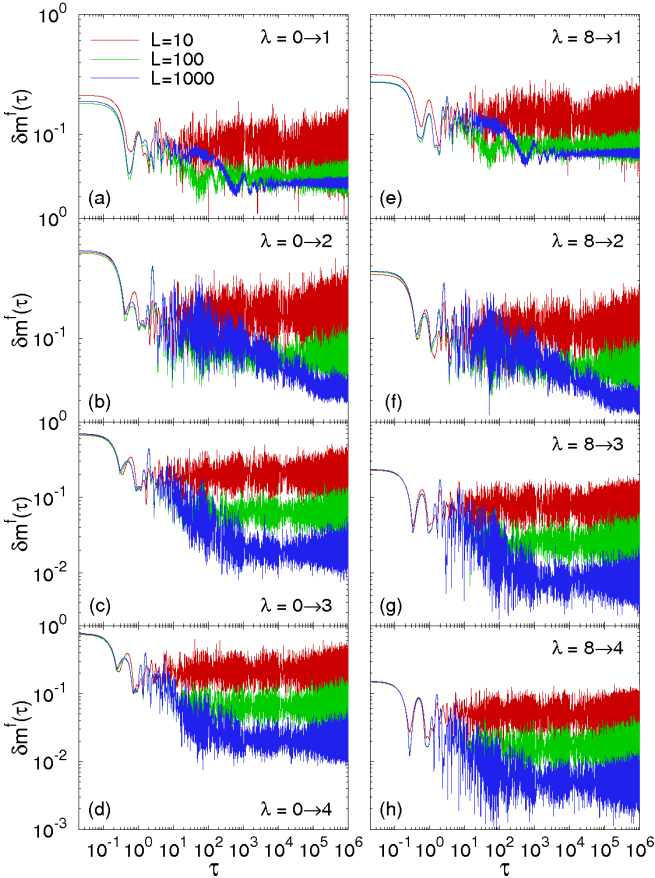


FIG. 1: (Color online) Relaxation dynamics of m_k^f in quenches $\lambda = \lambda_I \rightarrow \lambda_F$ (as indicated in the panels) for systems with 10, 100, and 1000 lattice sites (curves from top to bottom in each panel), and $N = L/2$.

The results obtained for a given final value of the incommensurate potential strength are qualitatively similar, independently of whether the initial state is delocalized or localized. In quenches to the localized regime [Figs. 1(c), (d), (g), (h)], we observe that $\delta m_k^f(\tau)$ decays to a finite value, about which it undergoes fluctuations, and that this value decreases with increasing system size. In quenches to the delocalized regime [Figs. 1(a) and 1(e)], $\delta m_k^f(\tau)$ similarly undergoes decay to a finite value about which it fluctuates. However, in the delocalized case, the value to which $\delta m_k^f(\tau)$ decays does not appear to exhibit such a pronounced reduction as the system size is increased, suggesting that it may not tend towards zero as $L \rightarrow \infty$. Following quenches to the critical point [Figs. 1(b) and 1(f)], $\delta m_k^f(\tau)$ exhibits behavior similar to that observed in the localized regime, decaying to exhibit fluctuations about a constant value which decreases with increasing system size. However, in this critical regime the decay of $\delta m_k^f(\tau)$ is much slower and, e.g., fluctuation about a constant value in the case $L = 1000$ is only obtained for $\tau \gtrsim 10^5$.

To gain a quantitative understanding of the dependence of the long-time behavior of Eq. (15) on the system size, we consider the average of $\delta m_k^f(\tau)$ over the time interval $\tau \in [10^5, 10^6]$, which we take as representative of the aver-

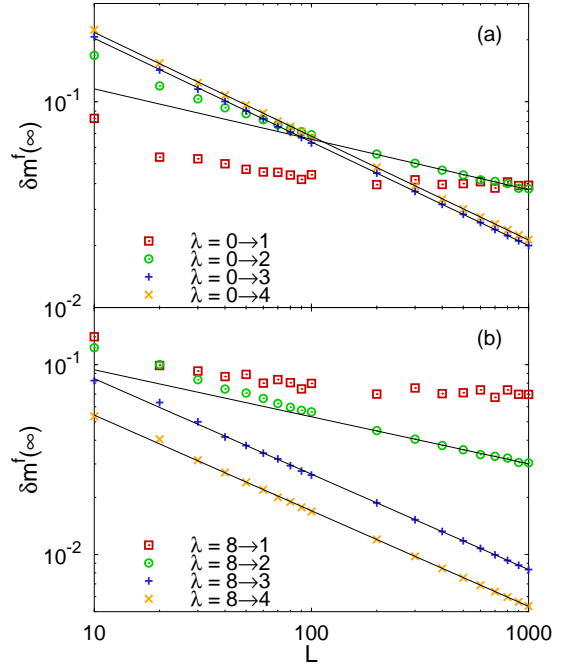


FIG. 2: (Color online) Finite-size scaling of $\delta m^f(\infty)$ (see text) for the quenches studied in Fig. 1. Thin continuous lines depict power-law fits in which $\delta m^f(\infty) \propto L^{-0.25 \pm 0.01}$ for quenches with $\lambda_F = \lambda_c$ and $\delta m^f(\infty) \propto L^{-0.500 \pm 0.005}$ in quenches with $\lambda_F > \lambda_c$. The power laws were fitted to results with L in the interval [200, 1000].

age value after any initial transient dynamics have subsided — such that $\delta m_k^f(\tau)$ is simply fluctuating about a constant value — and away from any revival, and denote this quantity by $\delta m^f(\infty)$. In Fig. 2, we plot $\delta m^f(\infty)$ against L for all the quenches shown in Fig. 1. The scalings make apparent that $\delta m^f(\infty)$ converges to a finite value as the system size is increased in quenches to the delocalized phase; i.e., although the infinite time average of each m_k^f trivially agrees with its expectation value in the GGE, its instantaneous value does not relax to the GGE in the thermodynamic limit. By contrast, in quenches to the localized regime $\delta m^f(\infty)$ decreases with increasing system size as a power-law, which we find to be close to $L^{-0.50}$. In the quenches to the critical regime, $\delta m^f(\infty)$ is much slower to reach a clear power law scaling, but for large system sizes its behavior is consistent with $\delta m^f(\infty) \propto L^{-0.25}$.

The behavior of $\delta m^f(\infty)$ in the delocalized and localized regimes is exactly opposite to that observed for the density in Ref. [33, 54]. There it was found that the normalized difference of the density $\delta n(\infty) \propto L^{-0.5}$ in quenches to the delocalized phase, whereas it converges to a finite value in quenches to the localized phase. Intuitively, the extended states in the delocalized regime of the quasi-disordered lattice can be thought of as states that are localized in momentum space. In fact, the correspondence between position (momentum) space results in the delocalized phase and momentum (position) space quantities in the localized phase can, in the case of free fermions, be seen to be an exact consequence of the well-known self-duality of the Aubry-André model [44]. We note also that the behavior of $\delta m^f(\infty)$ at the critical point

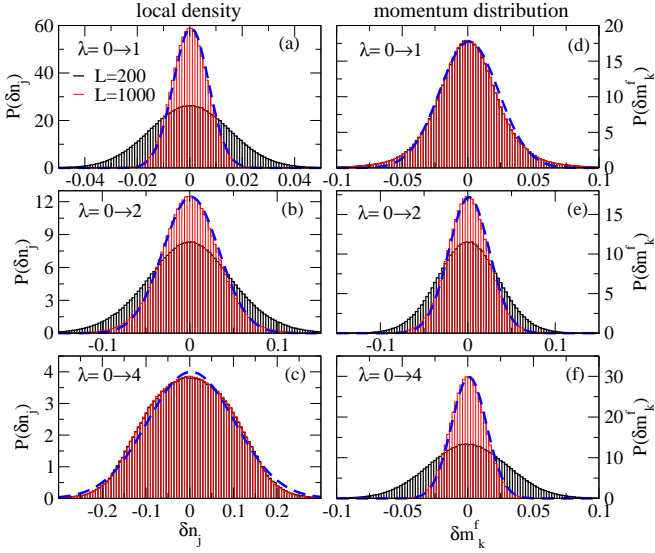


FIG. 3: (Color online) Histograms of the time fluctuations of n_j (left panels) and m_k^f (right panels) in quenches with $\lambda_I = 0$ and $\lambda_F = 1$ (a),(d), $\lambda_F = 2$ (b),(e), and $\lambda_F = 4$ (c),(f). In all panels, we report results for systems with $L = 200$ and $L = 1000$, and Gaussian fits to the data for $L = 1000$. From the fits, the means were found to be zero (± 0.003) in all cases and the variances were found to be $\sigma = (6.770 \pm 0.004) \times 10^{-3}$ (a), $(3.206 \pm 0.009) \times 10^{-2}$ (b), $(1.008 \pm 0.007) \times 10^{-1}$ (c), $(2.25 \pm 0.02) \times 10^{-2}$ (d), $(2.322 \pm 0.005) \times 10^{-1}$ (e), and $(1.336 \pm 0.001) \times 10^{-2}$ (f).

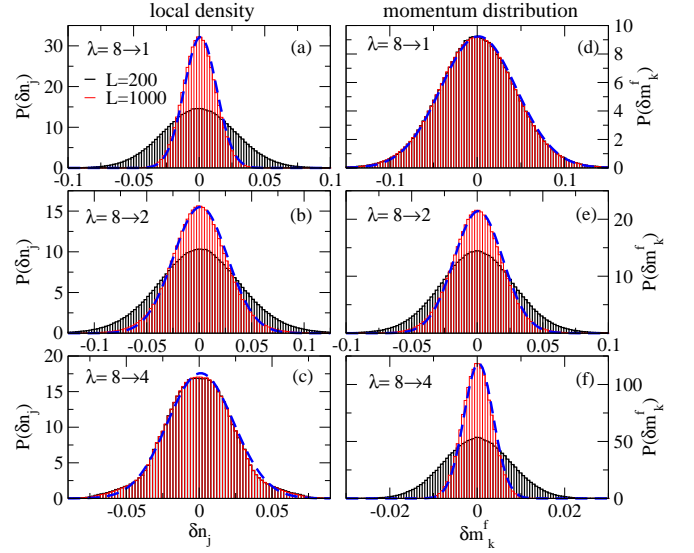


FIG. 4: (Color online) Histograms of the time fluctuations of n_j (left panels) and m_k^f (right panels) in quenches with $\lambda_I = 8$ and $\lambda_F = 1$ (a),(d), $\lambda_F = 2$ (b),(e), and $\lambda_F = 4$ (c),(f). In all panels, we report results for systems with $L = 200$ and $L = 1000$, and Gaussian fits to the data for $L = 1000$. From the fits, the means were found to be zero (± 0.003) in all cases and the variances were found to be $\sigma = (1.2373 \pm 0.0004) \times 10^{-2}$ (a), $(2.570 \pm 0.008) \times 10^{-2}$ (b), $(2.27 \pm 0.01) \times 10^{-2}$ (c), $(4.318 \pm 0.005) \times 10^{-2}$ (d), $(1.860 \pm 0.004) \times 10^{-2}$ (e), and $(3.360 \pm 0.003) \times 10^{-3}$ (f).

is similar to that found for $\delta n(\infty)$ in Ref. [33].

Aside from the peculiar behavior observed at the critical point, which is understandable given the very special character of the single-particle problem in this regime, it is remarkable that whenever relaxation of n_j or m_k^f takes place (in the delocalized or localized regime) the time fluctuations are proportional to $L^{-0.5}$. This is consistent with the Gaussian equilibration scenario of Ref. [40], in which the square root of the normalized time variance of one-body observables in noninteracting fermion systems was argued to scale as $1/\sqrt{L}$ [55].

In Figs. 3 and 4, we present histograms of the distributions of differences $\delta n_j(\tau) = n_j(\tau) - \langle \hat{n}_j \rangle_{\text{GGE}}$ between the instantaneous values of the site occupations and their mean values in the GGE (left panels), and the analogous quantities $\delta m_k^f(\tau) = m_k^f(\tau) - \langle \hat{m}_k^f \rangle_{\text{GGE}}$ calculated for momentum-mode occupations (right panels). These histograms represent the full distribution of fluctuations of the occupations of all lattice sites j , and all momentum modes k , in quenches with $\lambda_I = 0$ (Fig. 3) and $\lambda_I = 8$ (Fig. 4). Once again, the results for a given value of λ_F can be seen to be qualitatively similar independently of the initial state. The histograms of the time fluctuations of n_j in quenches to the delocalized regime and of m_k^f in quenches to the localized regime have a Gaussian shape with a width that decreases with increasing system size. By contrast, the histograms of the time fluctuations of n_j in quenches to the localized regime and of m_k^f in quenches to the delocalized regime are in general non-Gaussian (as can be seen by comparing them to the indicated best Gaussian fits

to the distributions) and the widths of the distributions are not seen to decrease with increasing system size. We note that the distributions of time fluctuations of *individual* lattice-site (momentum-mode) occupations in the localized (delocalized) phase, which we have not shown, are quite strongly non-Gaussian, exhibiting, e.g., bimodal structures. The behavior of the time fluctuations at the critical point is intermediate between what is seen in the localized and delocalized phases: The fluctuations of n_j and m_k^f are close to Gaussian, with a width that decreases less dramatically with increasing system size, consistent with the $L^{-0.25}$ behavior found for $\delta m^f(\infty)$ (Fig. 2). This exotic behavior at the critical point warrants a more specific investigation that is beyond the scope of this article.

An understanding of why Gaussian equilibration fails to occur for both fermionic observables at the critical point, for m_k^f in the delocalized phase, and for n_j in the localized one, can be gained through an analysis of the properties of the single-particle eigenstates of $\hat{H}_f(|s\rangle = \hat{\gamma}_s^\dagger |0\rangle)$ in both real and momentum space [30, 34, 35]. Since the variances

$$\begin{aligned} \sigma_{n_j}^2 &= \lim_{\tau' \rightarrow \infty} \frac{1}{\tau'} \int_0^{\tau'} d\tau [n_j(\tau) - \langle n_j \rangle_{\text{GGE}}]^2, \\ \sigma_{m_k^f}^2 &= \lim_{\tau' \rightarrow \infty} \frac{1}{\tau'} \int_0^{\tau'} d\tau [m_k^f(\tau) - \langle m_k^f \rangle_{\text{GGE}}]^2, \end{aligned} \quad (16)$$

can be written as

$$\begin{aligned}\sigma_{n_j}^2 &= \sum_{s \neq s'} |u_{js}|^2 |u_{js'}|^2 |\rho_{ss'}^I|^2, \\ \sigma_{m_k}^2 &= \sum_{s \neq s'} |v_{ks}|^2 |v_{ks'}|^2 |\rho_{ss'}^I|^2,\end{aligned}\quad (17)$$

where $\rho_{ss'}^I = \langle \Psi_I | \hat{\gamma}_s^\dagger \hat{\gamma}_{s'} | \Psi_I \rangle$, and $\hat{\gamma}_s^\dagger = \sum_j u_{js} \hat{f}_j^\dagger$ (\hat{c}_k^\dagger creates a SF at momentum k), it follows that [34]: (i) if $|s\rangle$ is delocalized in real (momentum) space then $|u_{js}|^2 \sim 1/L$ ($|v_{ks}|^2 \sim 1/L$) and $\sigma_{n_j}^2$ ($\sigma_{m_k}^2$) must decrease as $1/L$ or faster (because $\sum_{s,s'} |\rho_{ss'}^I|^2 = N_f$) with increasing system size, and (ii) if $|s\rangle$ is localized in real (momentum) space then the corresponding variance $\sigma_{n_j}^2$ ($\sigma_{m_k}^2$) will be dominated by rare large values of $|\rho_{ss'}^I|^2$ and will remain finite in the thermodynamic limit.

In the insets to Fig. 5, we plot the average of the square root of the variance over all lattice sites $\sigma_n^{\text{ave}} = 1/L \sum_j \sigma_{n_j}$ [insets in Fig. 5(a)] and over all momentum states $\sigma_m^{\text{ave}} = 1/L \sum_k \sigma_{m_k}$ [insets in Fig. 5(b)] against the system size L , for systems with between 10 and 1000 lattice sites and subject to the same quenches studied previously ($\lambda_I = 0$ in the top insets and $\lambda_I = 8$ in the bottom ones). The results for σ_n^{ave} and σ_m^{ave} can be seen to be qualitatively similar to those in Ref. [33] for $\delta n(\infty)$ and in Fig. 2 for $\delta m^f(\infty)$. In order to relate the behavior of the variances to the properties of the single-particle eigenstates $|s\rangle$ in real and momentum space, we compute the average inverse participation ratios (IPRs)

$$\begin{aligned}\text{IPR}_n &= \frac{1}{L} \sum_s \sum_j |u_{js}|^4, \\ \text{IPR}_m &= \frac{1}{L} \sum_s \sum_k |v_{ks}|^4.\end{aligned}\quad (18)$$

The results for the IPRs are reported in the main panels in Fig. 5. They show that, as expected, the eigenstates of the Hamiltonian are delocalized in real space ($\text{IPR}_n \sim 1/L$) and localized in momentum space ($\text{IPR}_m \sim L^0$) for $\lambda_F < 2$, and localized in real space ($\text{IPR}_n \sim L^0$) and delocalized in momentum space ($\text{IPR}_m \sim 1/L$) for $\lambda_F > 2$, which explains the behavior of the time fluctuations of the density and fermionic momentum distributions in the delocalized and localized regimes. For $\lambda_F = 2$, we find that $\text{IPR}_n \sim \text{IPR}_m \sim 1/\sqrt{L}$, illustrating the exotic structure of the eigenstates of the critical Hamiltonian in both real and momentum space. From this scaling we can infer that $|u_{js}|^2 \sim |v_{ks}|^2 \sim 1/L^{0.75}$ when $\lambda_F = 2$, implying that $\sigma_{n_j}^2$ and $\sigma_{m_k}^2$ decay like $1/\sqrt{L}$ or faster at the critical point, which is indeed consistent with the results of Fig. 2. We note also that in general, the average square-root variances and IPRs in the critical regime reach their exotic scaling limits at quite small values of L , compared to the behavior of $\delta m^f(\infty)$ at the critical point (Fig. 2). The unambiguous scaling at criticality seen in Fig. 5 thus lends strong support to our identification of $\delta m^f(\infty)$ as scaling like $\sim L^{-0.25}$.

For fermionic observables, we should stress the fact that, in the localized regime, localization in real space precludes re-

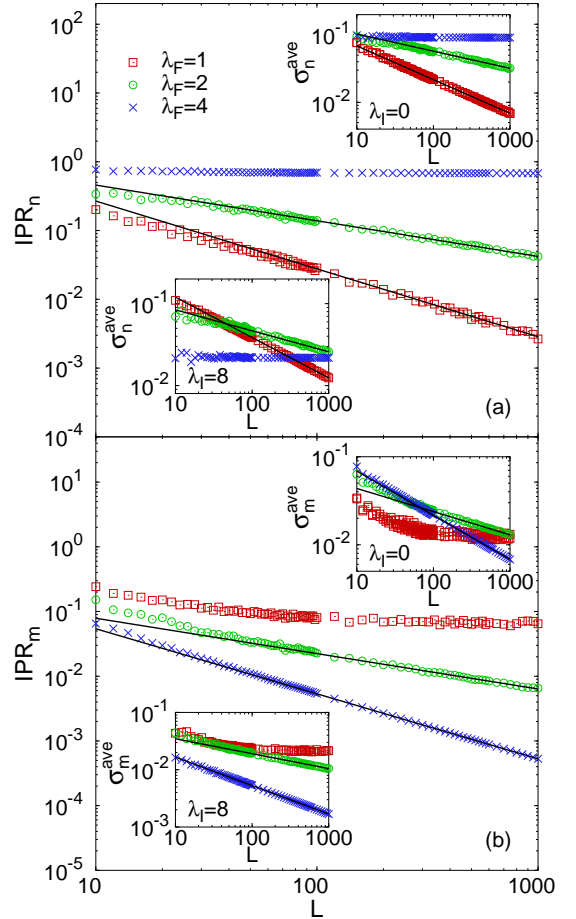


FIG. 5: (Color online) Inverse participation ratios in real (a) and momentum space (b) in the delocalized and localized phases as well as at the critical point. Thin continuous lines are power-law fits in which (a) $\text{IPR}_n \propto L^{-0.99 \pm 0.02}$ for $\lambda_F = 1$ and $\text{IPR}_n \propto L^{-0.52 \pm 0.01}$ for $\lambda_F = 2$, and (b) $\text{IPR}_m \propto L^{-0.55 \pm 0.01}$ for $\lambda_F = 2$ and $\text{IPR}_n \propto L^{-1.005 \pm 0.001}$ for $\lambda_F = 4$. The insets in (a) depict σ_n^{ave} for quenches with $\lambda_I = 0$ (top inset) and $\lambda_I = 8$ (bottom inset), while the insets in (b) depict σ_m^{ave} for quenches with $\lambda_I = 0$ (top inset) and $\lambda_I = 8$ (bottom inset). Thin continuous lines are power-law fits in which, in both insets in (a), $\sigma_n^{\text{ave}} \propto L^{-0.50 \pm 0.01}$ for $\lambda_F = 1$ and $\sigma_n^{\text{ave}} \propto L^{-0.25 \pm 0.01}$ for $\lambda_F = 2$, and, in both insets in (b), $\sigma_m^{\text{ave}} \propto L^{-0.25 \pm 0.02}$ for $\lambda_F = 2$ and $\sigma_m^{\text{ave}} \propto L^{-0.50 \pm 0.005}$ for $\lambda_F = 4$. The power laws were fitted to results with L in the interval [160, 1000].

laxation of the density profiles in the same way that, in the delocalized regime, localization in momentum space precludes relaxation of the momentum distribution. This symmetry between localization in real and momentum space is broken in the case of HCBs, because the mapping to the underlying model of SFs only preserves correlations that are diagonal in real space (i.e., properties related to the density). Thus for HCBs, although relaxation of the density is precluded in the localized regime, relaxation of the momentum distribution can occur in the delocalized regime, as was found in Ref. [33].

As discussed in Refs. [30, 34, 35], if the variances of one-particle correlations (here we have focused only on the density) do not vanish with increasing system size — which is

only possible if off-diagonal elements of $|\rho_{ss'}^I|^2$ contribute to the fluctuations in the thermodynamic limit — then Wick’s theorem can break down for time averages of higher order correlations. We recall that nonlocal one-particle correlations of HCBs [e.g., Eq. (7)] correspond, via the Jordan-Wigner transformation, to higher order correlations of SFs [35]. Thus the breakdown of the GGE for describing m_k^b after relaxation in the localized phase of HCBs [33] can be understood as a direct consequence of the fact that time fluctuations of local one-particle correlations of the underlying free-fermion model remain finite as one increases the system size in the localized phase.

IV. MANY-BODY ANALYSIS

In this section, we study the density profiles and momentum distribution functions in the many-body eigenstates of the SF and HCB Hamiltonians. Our goal is to understand how localization, in real and momentum space, affects the many-body eigenstate expectation values of these observables. Since this study requires the construction of the full set of energy eigenstates of the many-body system, which grows exponentially with increasing system size, our analysis will be restricted to lattice lengths that are much smaller than those studied in the single-particle analysis of the previous section. The smallest systems considered in this section have 20 sites and the largest ones have $L = 50$, with $N = L/5$, as opposed to the filling $N = L/2$ (which yields the maximal Hilbert space dimension for a given system size) considered in the previous section. The largest systems we consider have a Hilbert space of dimension $\mathcal{O}(10^{10})$. In order to compare systems that have equivalent excitation energies per particle after the quench, we will focus on three quenches that, while having the same final Hamiltonians as in the previous section, have for their initial states the respective ground states of Hamiltonians with $\lambda_I = -1.5$ for $\lambda_F = 1.0$, $\lambda_I = -0.5$ for $\lambda_F = 2.0$ and $\lambda_I = 1.0$ for $\lambda_F = 4.0$. These three quenches lead to time-evolving states whose energies are similar to those of systems in thermal equilibrium with $T \sim 1.7$.

In Fig. 6, we show the distribution of conserved quantities in the quenches mentioned above for systems with $L = 50$. We compare results for those distributions in the initial state (same as the DE and the GGE), in the GME (constructed as described in Sec. II), and in the ME. The contrast between the distribution of conserved quantities in the initial state and in the ME is apparent, whereas the distribution in the GME closely agrees with that in the initial state. Figures 6(d)–6(i) depict how the normalized absolute differences between the distribution of conserved quantities in the GME and ME and that in the initial state [Eq. (12) and the analogous expression obtained by replacing $\langle \hat{I}_s \rangle_{\text{GME}}$ with $\langle \hat{I}_s \rangle_{\text{ME}}$, respectively] scale with increasing system size. For the systems analyzed here, these differences are always smaller for the GME than for the ME. More importantly, for all quenches, they are seen to decrease with increasing system size for the GME [Figs. 6(d), 6(f), and 6(h)]. The differences between the ME and the DE exhibit clear saturation behavior in the de-

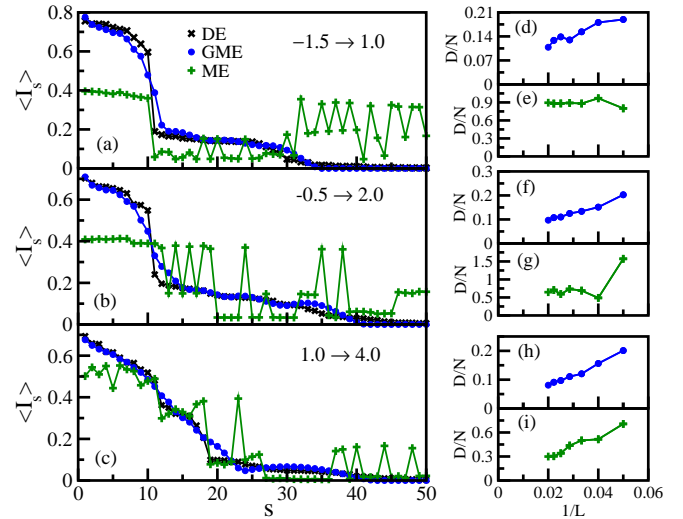


FIG. 6: (Color online.) [(a),(b),(c)] Conserved quantities $\langle I_s \rangle$ in the DE, GME, and ME for $L = 50$, $N = 10$, sorted in order of decreasing occupation in the DE. [(d)–(i)] Scaling of the absolute differences D between distributions of conserved quantities with increasing system size. [(d),(f),(h)] Absolute differences D between the conserved quantities in the GME and the DE [see Eq. (12)]. [(e),(g),(i)] D between the conserved quantities in the ME and the DE [same as Eq. (12) but with “GME”→“ME”]. The quenches are indicated as $\lambda_I \rightarrow \lambda_F$. For quenches $\lambda_I = -1.5 \rightarrow \lambda_F = 1.0$ and $\lambda_I = -0.5 \rightarrow \lambda_F = 2.0$ we found that $\delta_{\text{GME}} = 0.85$ yields the minimum value of D , and for quenches $\lambda_I = 1.0 \rightarrow \lambda_F = 4.0$ we found $\delta_{\text{GME}} = 0.95$. For the ME, $\delta_{\text{ME}} = 0.05$ in all quenches.

calized and critical regimes [Figs. 6(e), 6(g)]. In the localized regime [Figs. 6(i)], the difference between the ME and DE is both smaller than, and does not exhibit saturation quite as obviously as, that in the other two regimes. We note, however, that it was found previously in Ref. [28] that the discrepancy between distributions of conserved quantities in the ME and DE can be strongly dependent on the initial state (and in particular on its energy).

Although disagreement between the distributions of conserved quantities in the DE and ME indicates the failure of the ME to describe the state of the system after relaxation, the degree of agreement between the corresponding distributions in the DE and GME yields only incomplete information on the accuracy of the GGE as a characterization of the system at long times. In particular, the distributions here apply equally to SFs and HCBs, whereas the results of Ref. [33] and Sec. III indicate that the presence or absence of relaxation, and the agreement between time averages and the GGE predictions, can differ between SFs and HCBs with equal quench parameters. To further characterize the relationship between (generalized) thermalization and the structure of the many-body eigenstates of the system, we now turn our attention to the behavior of the density and momentum distributions in the eigenstates of the SF and HCB systems.

In order to quantify the differences between the predictions of the GME and ME for each observable and those of the DE,

we compute the normalized difference,

$$\Delta O^{\text{stat-DE}} = \frac{\sum_{\ell} |O_{\text{stat},\ell} - O_{\text{DE},\ell}|}{\sum_{\ell} O_{\text{DE},\ell}}, \quad (19)$$

where O is either the site occupation n (for which $\ell = j$) or the momentum occupation m^f , m^b (for which $\ell = k$), $O_{\text{stat},\ell} = \sum_{\alpha} w_{\alpha}^{\text{stat}} \langle \psi_{\alpha} | \hat{O}_{\ell} | \psi_{\alpha} \rangle \equiv \langle \hat{O}_{\ell} \rangle_{\text{stat}}$, with w_{α}^{stat} the weight of each many-body eigenstate in the relevant ensemble, and ‘stat’ stands for one of the three ensembles: the DE, the GME, or the ME. Hence, the agreement between a statistical ensemble and the DE in the thermodynamic limit becomes apparent if $\Delta O^{\text{stat-DE}}$ vanishes with increasing system size.

We quantify the behavior of the eigenstate expectation values of the observables by calculating the average variance within each ensemble, which we define by

$$\sigma_O^{\text{stat}} = \frac{\sum_{\ell} \sqrt{(O^2)_{\text{stat},\ell} - (O_{\text{stat},\ell})^2}}{L}, \quad (20)$$

where $(O^2)_{\text{stat},\ell} = \sum_{\alpha} w_{\alpha}^{\text{stat}} \langle \psi_{\alpha} | \hat{O}_{\ell} | \psi_{\alpha} \rangle^2 \neq \langle \hat{O}_{\ell}^2 \rangle_{\text{stat}}$. A finite value of $(\sigma_O^{\text{GME}}) \sigma_O^{\text{ME}}$ in the thermodynamic limit implies that (generalized) eigenstate thermalization does not occur. However, the vanishing of $(\sigma_O^{\text{GME}}) \sigma_O^{\text{ME}}$ is not a sufficient condition for (generalized) eigenstate thermalization to occur: The (GME) ME may still fail to describe observables after relaxation if the differences between the expectation values of observables in distinct eigenstates contributing to the ensemble do not vanish in the thermodynamic limit. In such a scenario, the results of the DE for the expectation values of observables may be dominated by ‘rare’ states, and thus be distinct from those of the (GME) ME [8]. We calculated the individual differences between observables in each eigenstate and in the ensemble average and attempted to quantify the scale of the maximal differences with increasing system size. However, the results were found to be dominated by finite size effects and we could not extract any consistent information from our investigations. We therefore only report results for σ_O^{stat} in this section.

We further note that, in a previous study of HCBs systems whose properties are qualitatively similar to those of the systems studied here for $\lambda < \lambda_c$ [28], indications were found that σ_m^{GME} (for m_k^b) vanishes with increasing system size while $\langle \hat{m}_k^b \rangle_{\text{GME}} = \langle \hat{m}_k^b \rangle_{\text{DE}}$. Since the weights w_{α}^{GME} and w_{α}^{DE} were seen to be different [28], with an exponentially smaller number of states usually contributing to the DE when compared to the GGE [56], the results of Ref. [28] hint that a generalized eigenstate thermalization may be at play for m_k^b . Namely, that all eigenstates with similar distributions of conserved quantities have similar expectation values of the HCB momentum distribution function (with differences that vanish in the thermodynamic limit).

We now present results that indicate that this mechanism is indeed the explanation why the GGE provides the correct description of HCB observables after relaxation in quenches to the delocalized phase. In Fig. 7, we show density plots of the coarse-grained weights with which eigenstates contribute to the DE [Fig. 7(a)] and to the GME [Fig. 7(b)] for delocalized HCB systems with $L = 45$ (main panels) and $L = 35$ (insets). The width of the windows used in the coarse graining is 0.005 in k and 0.002 in ε .

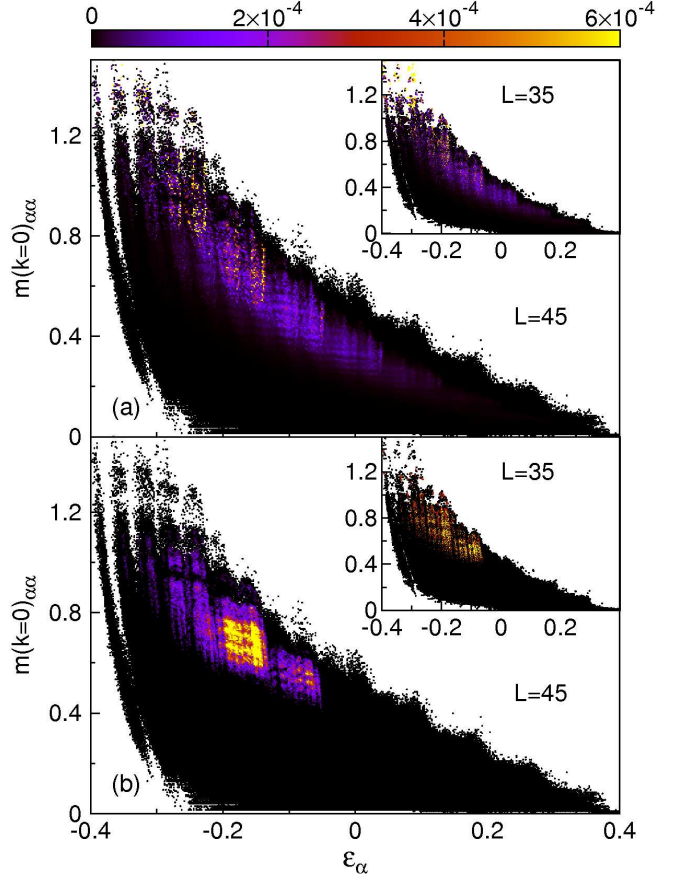


FIG. 7: (Color online.) Density plots of the coarse-grained weights of eigenstates in (a) the DE and (b) the GME as a function of the expectation value of $m(k = 0)$ and the eigenstate energy per site $\varepsilon_{\alpha} = E_{\alpha}/L$, for quenches to the delocalized regime. Results are shown for systems with $L = 45$ (main panel) and $L = 35$ (insets). The width of the windows used in the coarse graining is 0.005 in k and 0.002 in ε .

(insets). We see that in both ensembles, as the system size increases, weight becomes increasingly concentrated in eigenstates with $-1.0 < \varepsilon_{\alpha} \equiv E_{\alpha}/L < -0.5$ (though more clearly in the GME than in the DE). Moreover, the expectation values of $\hat{m}(k = 0)$ in these most highly weighted eigenstates are narrowly distributed compared to the full range of expectation values of all eigenstates within the same energy range. Furthermore, it is remarkable that the expectation values of $\hat{m}(k = 0)$ in the dominant states of the two ensembles are similar to each other, and that this agreement is seen to improve with increasing system size.

In Fig. 8 we present the corresponding results for quenches to the localized phase. We observe qualitative differences between the distributions of weights in the DE and in the GME: the former are spread relatively smoothly over energies $\varepsilon_{\alpha} < 2$ [Fig. 8(a)], whereas the latter tend to concentrate in several distinct energy bands [Fig. 8(b)]. Moreover, in the DE the weights tend to increase as ε_{α} decreases, corresponding to larger values of the expectation of $\hat{m}(k = 0)$, whereas in the GME the weight distribution is more strongly concentrated

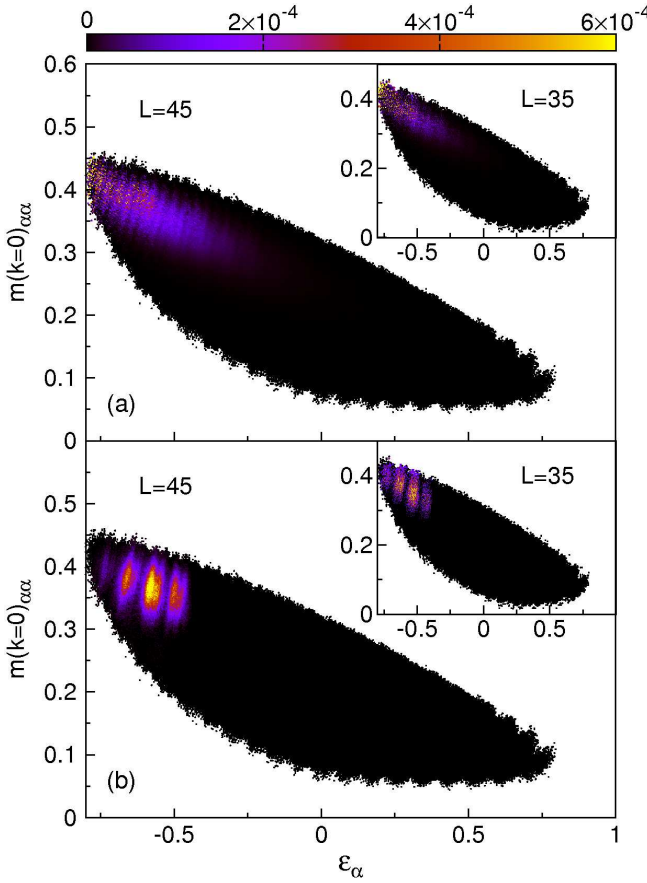


FIG. 8: (Color online.) Density plots of the coarse-grained weights of eigenstates in (a) the DE and (b) the GME as a function of $m(k=0)$ and the eigenstate energy per site $\varepsilon_\alpha = E_\alpha/L$, for quenches to the localized regime. Results are shown for systems with $L = 45$ (main panel) and $L = 35$ (insets). The width of the windows used in the coarse graining is 0.001 in k and 0.004 in ε .

in eigenstates with higher values of ε_α , and smaller values of the zero-momentum expectation values. This suggests that the dominant eigenstates in each of the two ensembles do not yield similar momentum distribution functions, implying the failure of generalized eigenstate thermalization in the localized phase, similar to the failure of eigenstate thermalization in nonintegrable systems in the presence of localization [39].

In what follows, we explore in more detail the properties of the eigenstate expectation values of the various observables of interest for SFs and HCBs, and how they change with increasing system size.

Quenches to the delocalized regime

We start by studying the behavior of the density profiles in the many-body eigenstates of the SF and HCB Hamiltonians. The density profiles of SFs and HCBs are identical, and, by construction, the predictions of the GGE for expectation value of this observable are the same as those of the DE.

In Fig. 9(a), we show the density profiles after a quench

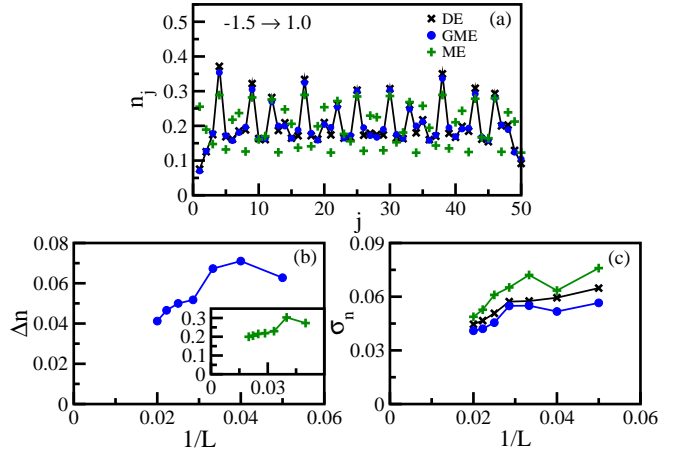


FIG. 9: (Color online.) (a) Density profiles ($L = 50$), (b) $\Delta n_i^{\text{stat-DE}}$, and (c) σ_n^{stat} in quenches to the delocalized regime, $\lambda_I = -1.5 \rightarrow \lambda_F = 1.0$. In (b), the main panel depicts $\Delta n_i^{\text{GME-DE}}$, while the inset depicts $\Delta n_i^{\text{ME-DE}}$. The legends for the ensembles considered are the same in all panels and are reported in (a). The values of δ_{GME} and δ_{ME} are the same for all L 's and are equal to the ones in Fig. 6.

to the delocalized regime as predicted by the DE, the GME, and the ME. The agreement between DE and GME is excellent, leading to the small values of $\Delta n_i^{\text{GME-DE}}$ in Fig. 9(b). The latter quantity is seen to decrease with increasing system size indicating that the DE and GME predictions will agree in the thermodynamic limit. On the other hand, in Fig. 9(a), large differences can be seen between the outcomes of DE and ME calculations for the density profiles, which leads to large values of $\Delta n_i^{\text{ME-DE}}$ as depicted in the inset in Fig. 9(b). The results in the inset suggest that $\Delta n_i^{\text{ME-DE}}$ saturates to a finite value with increasing L , which would be consistent with the results of Ref. [33], where the grand-canonical ensemble was shown to fail to predict the outcome of the relaxation dynamics with increasing system size for this observable (for systems up to 20 times larger than those considered here).

Figure 9(c) shows the scaling of the average variance of the site occupations in the DE, the GME, and the ME with L . In all ensembles, this variance is of a similar small magnitude, and decreases with increasing system size. However, our results are not conclusive as to whether the variance (in any of the ensembles) vanishes or saturates to a finite value in the thermodynamic limit. Inasmuch as we understand thermalization in an isolated system to result from eigenstate thermalization, the fact that this observable does not thermalize [33] implies that eigenstate thermalization does not occur in this system. Given the fact that the predictions of the GGE and GME for this observable agree with that of the DE, what remains to be clarified in future studies is whether the generalized eigenstate thermalization scenario is valid or not for n_j .

In Fig. 10, we present a study equivalent to the one in Fig. 9, but for the momentum distributions of SFs and HCBs. The first feature that is apparent in Figs. 10(a) and 10(d) is the contrast between the shape of momentum distribution of SFs and HCBs. For small values of k , the former resembles a Fermi sea and the latter resembles a bosonic system, both systems at

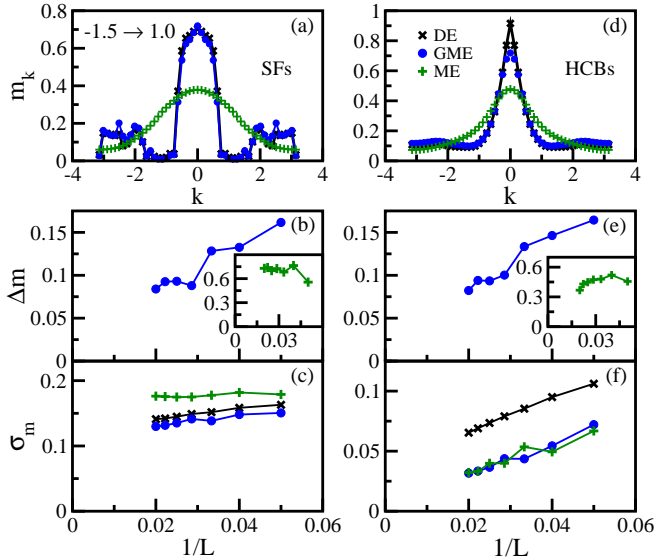


FIG. 10: (Color online.) [(a),(d)] Momentum distribution functions ($L = 50$), [(b),(e)] $\Delta m^{\text{stat-DE}}$, and [(c),(f)] σ_m^{stat} , for SFs (left column) and HCBs (right column), in quenches to the delocalized regime, $\lambda_I = -1.5 \rightarrow \lambda_F = 1.0$. In [(b),(e)], the main panels depict $\Delta m^{\text{GME-DE}}$, while the insets depict $\Delta m^{\text{ME-DE}}$. The legends for the ensembles considered are the same in all panels and are reported in (d). The values of δ_{GME} and δ_{ME} are the same for all L 's and are equal to the ones in Fig. 6.

finite but low temperature [52]. However, the high occupation of m_k^f and m_k^b in the tails makes it evident that the systems are not in thermal equilibrium, as can be seen by comparing them to the predictions of the ME. By contrast, the GME predictions for the momentum distributions closely agree with the DE results. This is better seen in Figs. 10(b) and 10(e), where the differences between the GME and the DE predictions are seen to be small and decrease with increasing system size. The insets to the same panels show that $\Delta m^{\text{ME-DE}}$ is several times larger than $\Delta m^{\text{GME-DE}}$ for the system sizes studied, and that the fermionic $\Delta m^{\text{ME-DE}}$ has a tendency to saturate to a finite value as $L \rightarrow \infty$, though the behavior of $\Delta m^{\text{ME-DE}}$ for HCBs is less clear.

The results for the scaling of σ_m^{stat} with increasing system size [Fig. 10(c) and 10(f)] make apparent a fundamental difference between the behavior of eigenstate expectation values of \hat{m}_k^f and \hat{m}_k^b . For all ensembles, σ_m^{stat} for SFs [Fig. 10(c)] is seen to be larger than the corresponding variance σ_m^{stat} for HCBs [Fig. 10(f)], and the former appears to saturate to a finite value (more clearly seen within the ME than within the DE and the GME), while the latter appears to vanish (more clearly seen within the GME and the ME than within the DE) in the thermodynamic limit. This makes evident that localization of the single-particle fermionic eigenstates in momentum space has a clear consequence on the behavior of m_k^f in the many-body eigenstates, for which σ_m^{stat} may be finite in the thermodynamic limit. By contrast, such a localization phenomenon in the single-particle basis appears not to have any effect on the many-body eigenstate expectation values of

the momentum distribution of the HCBs, for which *generalized* eigenstate thermalization can take place as σ_m^{stat} appears to vanish for all ensembles, and $\langle \hat{m}_k^b \rangle_{\text{DE}} = \langle \hat{m}_k^b \rangle_{\text{GME}}$ [33]. Again, we stress that even if the bosonic σ_m^{ME} does vanish in the thermodynamic limit, we can infer that eigenstate thermalization does not occur for m_k^b from the failure of thermalization to occur for this observable [33].

Quenches to the localized regime

Density profiles obtained within the DE, GME, and ME after a quench to the localized regime are shown in Fig. 11(a), and the scalings of $\Delta n^{\text{GME-DE}}$ ($\Delta n^{\text{ME-DE}}$) with increasing system size are reported in the main panel (inset) in Fig. 11(b). Despite the fact that the site occupations fluctuate from site to site much more in Fig. 11(a) than in Fig. 9(a), the GME results still closely agree with those of the DE, while the ME results do not. The scaling of $\Delta n^{\text{GME-DE}}$ with increasing system size suggests that the differences between the predictions of the GME and the DE will vanish in the thermodynamic limit. The results for $\Delta n^{\text{ME-DE}}$ are less conclusive, although the values of this quantity obtained for the largest system sizes suggest a possibly tendency toward saturation.

A clear difference between the behavior of the site occupations in the localized and delocalized regimes is seen in the fact that the variance of the eigenstate expectation values of this observable saturates in all three ensembles to a finite value in the former [Fig. 11(c)], whereas our results suggest that it vanishes in the latter [Fig. 9(c)], as the system size is increased. The saturation observed in Fig. 11(c) is a clear consequence of localization of the single-particle eigenstates in real space for $\lambda > \lambda_c$. Finite values of the fermionic σ_m^{ME} in the delocalized regime and of σ_n^{ME} in the localized one are

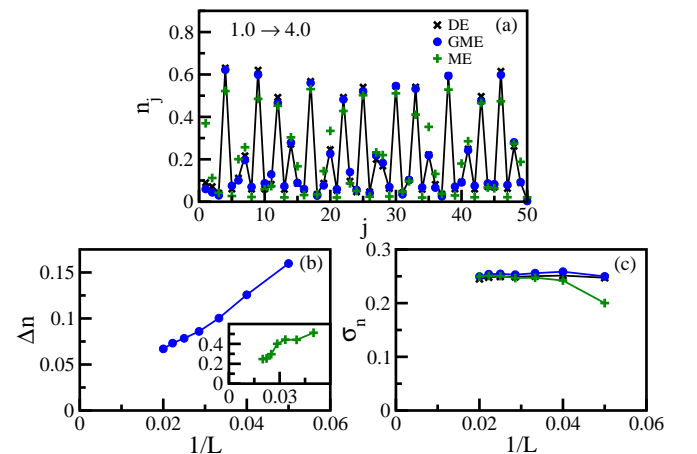


FIG. 11: (Color online.) (a) Density profiles ($L = 50$), (b) $\Delta n^{\text{stat-DE}}$, and (c) σ_n^{stat} in quenches to the localized regime, $\lambda_I = 1.0 \rightarrow \lambda_F = 4.0$. In (b), the main panel depicts $\Delta n^{\text{GME-DE}}$, while the inset depicts $\Delta n^{\text{ME-DE}}$. The legends for the ensembles considered are the same in all panels and are reported in (a). The values of δ_{GME} and δ_{ME} are the same for all L 's and are equal to the ones in Fig. 6.

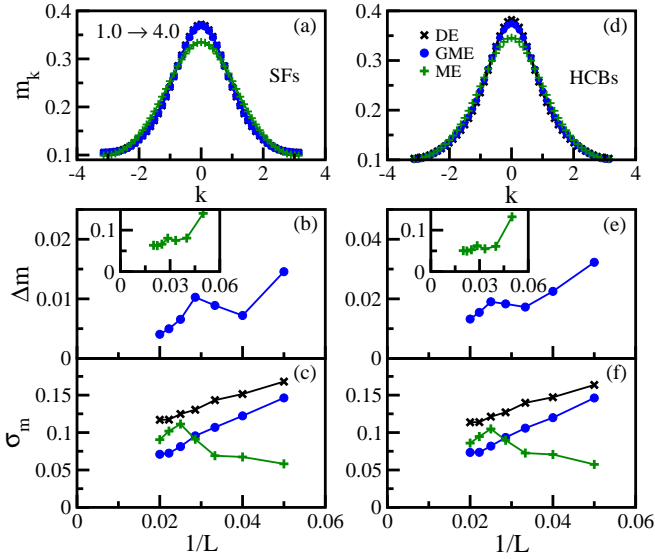


FIG. 12: (Color online.) [(a),(d)] Momentum distribution functions ($L = 50$), [(b),(e)] $\Delta m^{\text{stat-DE}}$, and [(c),(f)] σ_m^{stat} , for SFs (left column) and HCBs (right column), in quenches to the localized regime, $\lambda_I = 1.0 \rightarrow \lambda_F = 4.0$. In [(b),(e)], the main panels depict $\Delta m^{\text{GME-DE}}$, while the insets depict $\Delta m^{\text{ME-DE}}$. The legends for the ensembles considered are the same in all panels and are reported in (d). The values of δ_{GME} and δ_{ME} are the same for all L 's and are equal to the ones in Fig. 6.

physically relevant examples of the failure of the variance of few-body observables in the many-body eigenstates that constitute the ME to vanish in the thermodynamic limit, contrary to what is generally expected to occur for few-body observables [8].

In Figs. 12(a) and 12(d), we show the momentum distribution functions of SFs and HCBs in the DE, the GME, and the ME after a quench to the localized regime. In each ensemble the results for SFs and HCBs are barely distinguishable from each other, which we might intuitively attribute to localization undermining the particle statistics. As in the quenches to the delocalized regime, the GME results closely follow those of the DE, and the main panels in Figs. 12(b) and 12(e) indicate that $\Delta m^{\text{GME-DE}}$ decreases with increasing system size. Whereas we expect $\Delta m^{\text{GME-DE}}$ to vanish for SFs in the thermodynamic limit (as the DE and GGE predictions coincide for all one-body fermionic observables), for HCBs we expect it to converge to a small but finite value, because of the failure of the GGE to describe the time averages of the HCB momentum distribution function observed in Ref. [33]. In Figs. 12(a) and 12(d), the ME results for the momentum distributions are clearly distinct from those of the DE, and that difference is expected to remain in the thermodynamic limit both for SFs and HCBs, as suggested by the scaling of $\Delta m^{\text{ME-DE}}$ in the insets in Figs. 12(b) and 12(e).

Results for the scaling of σ_m^{stat} with increasing system size are presented in Figs. 12(c) and 12(f), for SFs and HCBs, respectively. Once again, the results for the two particle species are very similar to each other. They are particularly inconclu-

sive for σ_m^{ME} , which is seen to increase with increasing system size for all systems except the two largest ones, for which it is seen to decrease. On the other hand, σ_m^{DE} and σ_m^{GME} decrease for all system sizes, though the results for the largest two system sizes suggest that they may saturate. This leaves open the question of whether σ_m^{stat} vanishes in the thermodynamic limit or whether it remains finite. What is clear from the fact that both the GE and the GGE fail to describe m_k^b after relaxation [33] is that neither eigenstate thermalization nor generalized eigenstate thermalization take place in the HCB system in this regime.

Quenches to the critical point

For completeness, we present here results for the ensemble expectation values of observables in quenches to the critical point. We note that from the analyses of Sec. III and Ref. [33], we expect the critical regime to be most sensitive to finite size effects.

In Fig. 13 we present results for the density profiles. They are in between those for quenches to the delocalized and localized phases, as expected due to the finite and small nature of the lattice sizes studied. In particular, the average variance σ_n^{stat} decreases with increasing system size but has a tendency to saturate, so much larger system sizes will be needed to resolve whether it vanishes in the thermodynamic limit (as it may in quenches to the delocalized phase) or whether it remains finite (as expected from the observed behavior in quenches to the localized phase).

Figure 14 shows results for the momentum distribution functions of SFs (left columns) and HCBs (right columns). They are also intermediate between those obtained in the delocalized and localized regimes. The average variance σ_m^{stat} is

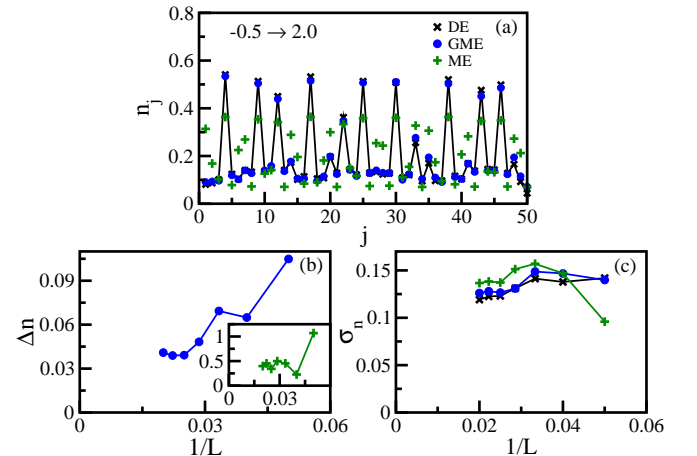


FIG. 13: (Color online.) (a) Density profiles ($L = 50$), (b) $\Delta n^{\text{stat-DE}}$, and (c) σ_n^{stat} in quenches to the critical point, $\lambda_I = -0.5 \rightarrow \lambda_F = 1.0$. In (b), the main panel depicts $\Delta n^{\text{GME-DE}}$, while the inset depicts $\Delta n^{\text{ME-DE}}$. The legends for the ensembles considered are the same in all panels and are reported in (a). The values of δ_{GME} and δ_{ME} are the same for all L 's and are equal to the ones in Fig. 6.

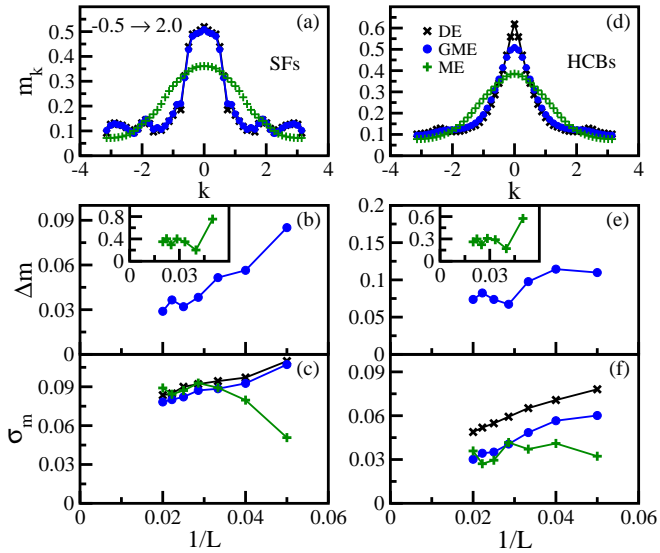


FIG. 14: (Color online.) [(a),(d)] Momentum distribution functions ($L = 50$), [(b),(e)] $\Delta m^{\text{stat-DE}}$, and [(c),(f)] σ_m^{stat} , for SFs (left column) and HCBs (right column), in quenches to the critical point, $\lambda_I = -0.5 \rightarrow \lambda_F = 1.0$. In [(b),(e)], the main panels depict $\Delta m^{\text{GME-DE}}$, while the insets depict $\Delta m^{\text{ME-DE}}$. The legends for the ensembles considered are the same in all panels and are reported in (d). The values of δ_{GME} and δ_{ME} are the same for all L 's and are equal to the ones in Fig. 6.

larger for SFs than for HCBs, as in the delocalized phase. It can also be seen to decrease with increasing system size (as it does in the localized phase), but has a tendency to saturate (as it does in the delocalized phase), so much larger system sizes will be needed to resolve whether it vanishes or remains finite in the thermodynamic limit.

V. SUMMARY

We have studied the dynamics of the momentum distribution function of noninteracting spinless fermions following quenches to the delocalized, localized, and critical regimes of a quasi-disordered lattice system. We found that although the time-averaged value of this observable agrees exactly with the predictions of the GGE in all three regimes, it does not exhibit relaxation after a quench in the delocalized phase. This is complementary to the failure of the on-site density of hard-core bosons (and therefore the noninteracting fermion system considered here) to equilibrate that was previously observed in Ref. [33]. These behaviors can be understood in terms of localization of the single-particle eigenstates of the fermion model, in momentum space for the delocalized regime, and in real space for the localized regime, as discussed in Refs. [30, 34, 35]. This analysis also helps us to understand the failure of the GGE to describe the momentum distribution functions of HCBs after relaxation in the localized regime ob-

served in Ref. [33] as a consequence of non-vanishing time fluctuations of one-particle fermionic correlations that persist in the thermodynamic limit.

We found that in the delocalized and localized regimes, the SF observables that do exhibit relaxation to the GGE — the density in the former case, and the momentum distribution function in the latter — do so in a manner consistent with the Gaussian equilibration picture of Campos Venuti and Zanardi [40]. In quenches to the critical point of the Aubry-André model, we observed that both the density and the momentum distribution function of SFs exhibit equilibration to the GGE, but that the decay of the time fluctuations of these quantities with increasing system size is slower than that predicted by the conjecture of Ref. [40].

We also studied the expectation values of one-body observables in the many-body eigenstates of the SF and HCB Hamiltonians, comparing results for the diagonal, microcanonical, and generalized microcanonical ensembles. Our observations indicate that the single-particle localization — in momentum space in the delocalized regime and in real space in the localized regime — that precludes relaxation of the corresponding observables to the GGE also leads to finite thermodynamic-limit variances of momentum and site occupations, respectively, in the many-body eigenstates of the SF Hamiltonian. By contrast, the failure of the GGE to describe the momentum distribution of HCBs after relaxation in the localized phase was not found to be associated with any corresponding saturation of the variance of momentum occupations in eigenstates of the HCB Hamiltonian with increasing system size.

Because of finite-size effects, we did not find clear indications of the behavior of the maximum difference between the expectation values of the density and momentum distribution in all the eigenstates contributing to the ensemble averages as the system sizes is increased. It would be particularly important to understand whether the values of observables in the individual eigenstates constituting the GME approach their average values in this ensemble with increasing system size, in order to clarify whether generalized eigenstate thermalization occurs in the delocalized regime — which would explain why the GGE works there for describing the momentum distribution functions of HCBs after relaxation — and whether generalized eigenstate thermalization fails (as we expect) in the localized regime, where the GGE fails. It would also be interesting to see how the addition of nearest neighbor interactions [57], which break integrability, modify our findings for both SFs and HCBs.

Acknowledgments

This work was supported by the Office of Naval Research (K.H., L.F.S., and M.R.), by NSF grant No. DMR-1147430 (L.F.S.), by ARC Discovery Project Grant No. DP110101047 (T.M.W.), and partially under KITP NSF grant No. PHY11-25915 (L.F.S., T.M.W., and M.R.).

[1] I. Bloch, J. Dalibard, and W. Zwerger, *Rev. Mod. Phys.* **80**, 885 (2008).

[2] M. A. Cazalilla, R. Citro, T. Giamarchi, E. Orignac, and M. Rigol, *Rev. Mod. Phys.* **83**, 1405 (2011).

[3] J. M. Deutsch, *Phys. Rev. A* **43**, 2046 (1991).

[4] M. Srednicki, *Phys. Rev. E* **50**, 888 (1994).

[5] M. Rigol, V. Dunjko, and M. Olshanii, *Nature* **452**, 854 (2008).

[6] M. Rigol, *Phys. Rev. Lett.* **103**, 100403 (2009).

[7] M. Rigol, *Phys. Rev. A* **80**, 053607 (2009).

[8] G. Biroli, C. Kollath, and A. M. Läuchli, *Phys. Rev. Lett.* **105**, 250401 (2010).

[9] C. Neuenhahn and F. Marquardt, *Phys. Rev. E* **85**, 060101 (2012).

[10] R. Steinigeweg, J. Herbrych, and P. Prelovšek, *Phys. Rev. E* **87**, 012118 (2013).

[11] L. F. Santos and M. Rigol, *Phys. Rev. E* **81**, 036206 (2010).

[12] L. F. Santos and M. Rigol, *Phys. Rev. E* **82**, 031130 (2010).

[13] M. Horoi, V. Zelevinsky, and B. A. Brown, *Phys. Rev. Lett.* **74**, 5194 (1995); N. Frazier, B. A. Brown and V. Zelevinsky, *Phys. Rev. C* **54**, 1665 (1996).

[14] V. Zelevinsky, B. A. Brown, N. Frazier, and M. Horoi, *Phys. Rep.* **276**, 85 (1996).

[15] V. V. Flambaum, F. M. Izrailev, and G. Casati, *Phys. Rev. E* **54**, 2136 (1996).

[16] V. V. Flambaum and F. M. Izrailev, *Phys. Rev. E* **56**, 5144 (1997).

[17] F. Borgonovi, I. Guarneri, F. M. Izrailev, and G. Casati, *Phys. Lett. A* **247**, 140 (1998); F. Borgonovi and F. M. Izrailev, *Phys. Rev. E* **62**, 6475 (2000).

[18] F. M. Izrailev, *Physica Scripta* **T90**, 95 (2001).

[19] M. Rigol, V. Dunjko, V. Yurovsky, and M. Olshanii, *Phys. Rev. Lett.* **98**, 050405 (2007).

[20] M. Rigol, A. Muramatsu, and M. Olshanii, *Phys. Rev. A* **74**, 053616 (2006).

[21] M. A. Cazalilla, *Phys. Rev. Lett.* **97**, 156403 (2006).

[22] P. Calabrese and J. Cardy, *J. Stat. Mech. p* P06008 (2007).

[23] M. Kollar and M. Eckstein, *Phys. Rev. A* **78**, 013626 (2008).

[24] A. Iucci and M. A. Cazalilla, *Phys. Rev. A* **80**, 063619 (2009).

[25] A. Iucci and M. A. Cazalilla, *New J. Phys.* **12**, 055019 (2010).

[26] J. Mossel and J.-S. Caux, *New J. Phys.* **12**, 055028 (2010).

[27] D. Fioretto and G. Mussardo, *New J. Phys.* **12**, 055015 (2010).

[28] A. C. Cassidy, C. W. Clark, and M. Rigol, *Phys. Rev. Lett.* **106**, 140405 (2011).

[29] P. Calabrese, F. H. L. Essler, and M. Fagotti, *Phys. Rev. Lett.* **106**, 227203 (2011).

[30] M. A. Cazalilla, A. Iucci, and M.-C. Chung, *Phys. Rev. E* **85**, 011133 (2012).

[31] P. Calabrese, F. H. L. Essler, and M. Fagotti, *J. Stat. Mech.* **2012**, P07022 (2012).

[32] P. Calabrese, F. H. L. Essler, and M. Fagotti, *J. Stat. Mech.* **2012**, P07016 (2012).

[33] C. Gramsch and M. Rigol, *Phys. Rev. A* **86**, 053615 (2012).

[34] S. Ziraldo, A. Silva, and G. E. Santoro, *Phys. Rev. Lett.* **109**, 247205 (2012).

[35] S. Ziraldo and G. E. Santoro, *Phys. Rev. B* **87**, 064201 (2013).

[36] E. T. Jaynes, *Phys. Rev.* **106**, 620 (1957).

[37] E. T. Jaynes, *Phys. Rev.* **108**, 171 (1957).

[38] J.-S. Caux and F. H. L. Essler, arXiv:1301.3806.

[39] E. Khatami, M. Rigol, A. Relaño, and A. M. García-García, *Phys. Rev. E* **85**, 050102 (2012).

[40] L. Campos Venuti and P. Zanardi, *Phys. Rev. E* **87**, 012106 (2013).

[41] T. Holstein and H. Primakoff, *Phys. Rev.* **58**, 1098 (1940).

[42] P. Jordan and E. Wigner, *Z. Phys.* **47**, 631 (1928).

[43] S. Aubry and G. André, *Ann. Isr. Phys. Soc.* **3**, 1335 (1980).

[44] J. B. Sokoloff, *Phys. Rep.* **126**, 189 (1985).

[45] A. M. Rey, I. I. Satija, and C. W. Clark, *Phys. Rev. A* **73**, 063610 (2006).

[46] K. He, I. I. Satija, C. W. Clark, A. M. Rey, and M. Rigol, *Phys. Rev. A* **85**, 013617 (2012).

[47] N. Nessi and A. Iucci, *Phys. Rev. A* **84**, 063614 (2011).

[48] D. R. Hofstadter, *Phys. Rev. B* **14**, 2239 (1976).

[49] M. Rigol and A. Muramatsu, *Phys. Rev. A* **70**, 031603(R) (2004).

[50] M. Rigol and A. Muramatsu, *Phys. Rev. A* **72**, 013604 (2005).

[51] K. He and M. Rigol, *Phys. Rev. A* **83**, 023611 (2011).

[52] M. Rigol, *Phys. Rev. A* **72**, 063607 (2005).

[53] M. Olshanii, arXiv:1208.0582.

[54] Note that the notation used in Ref. [33] differs somewhat from that used here. In particular, in Ref. [33], $\delta O(\tau)$ denotes the normalized difference between an instantaneous observable and its long-time average (which may not be the GGE value, in general), and ΔO^{GGE} is used to denote the normalized difference between the long-time average and the GGE prediction [corresponding to the notations $\delta n(\infty)$ and $\delta m^f(\infty)$ used here].

[55] The time averages of the normalized absolute differences calculated here are a lower bound to the square roots of the normalized variances considered in Ref. [40].

[56] L. F. Santos, A. Polkovnikov, and M. Rigol, *Phys. Rev. Lett.* **107**, 040601 (2011).

[57] S. Iyer, V. Oganesyan, G. Refael, and D. A. Huse, *Phys. Rev. B* **87**, 134202 (2013).